




Second harmonic injection locking of coupled spin torque vortex oscillators with an individual phase access

Leandro Martins ^{1,2}, Alex S. Jenkins ¹✉, Jérôme Borme ¹, João Ventura², Paulo P. Freitas¹ & Ricardo Ferreira¹

The synchronisation of magnetic tunnel junctions in the high frequency domain has attracted significant interest in the context of novel computation paradigms, specifically neuromorphic spintronics and probabilistic computing. In this work, a design for the coupling and synchronization of spin torque vortex oscillators (STVOs) is implemented. The geometry comprises the fabrication of adjacent pairs of STVO nanopillars (MgO-based magnetic tunnel junctions), with an edge-to-edge distance down to 100 nm, together with individual top contacts that allow an independent electrical access to each device. In this geometry, the magneto-dipolar coupling promotes the synchronization of the two oscillators, at the same time as the access to the frequency and phase of each individual oscillator is possible. Both frequency and time domain measurements confirm a successful synchronization, with the coupling being controlled by the relative DC bias in each oscillator. As a proof-of-concept towards an oscillator-based Ising machine, it is also shown that the second harmonic injection locking of an STVO can be controlled by tuning the magneto-dipolar coupling to its correspondent STVO pair. These results represent a step forward for the implementation of magneto-dipolar coupled magnetic tunnel junctions, specifically in the field of unconventional computing hardware.

¹INL, Avenida Mestre José Veiga, s/n, 4715-330 Braga, Portugal. ²IFIMUP-IN, Rua do Campo Alegre, 678, 4169-007 Porto, Portugal. ✉email: alex.jenkins@inl.int

Over the years, the synchronization of spin torque nano-oscillators (STNOs) has been a fundamental subject in Spintronics^{1–10}. At first, the main motivation was the possibility to improve the performance of STNOs^{11,12}, namely their output power and spectral coherence. Different successful approaches have been implemented, showing short range synchronization of adjacent STNOs (<1 μm) via spin wave propagation^{1,2,4,5} and magneto-dipolar coupling^{6,8,13} or a long range synchronization via mutual electric coupling^{7,9,10,14}.

Naturally, this progress made synchronization an attractive phenomenon to be implemented in some emergent spintronic fields, with neuromorphic computing being a notable example¹⁵. In the recent years, spintronic devices have been proposed for the hardware implementation of neuromorphic computing systems^{16–20}. Non-trivial tasks, such as vowel recognition, were achieved in a synchronization-based computing system¹⁷, where the recognition is performed based on the synchronization state between the input signal and a chain of four STNOs working as artificial neurons.

More recently, Albertsson et al. have proposed a network of synchronized STNOs working as an Ising machine to solve combinatorial optimization problems²¹. Specifically, it is numerically shown that the solution for a non-deterministic polynomial-hard-time (NP-hard) problem²², such as the Max-Cut problem²³, can be found by monitoring the second harmonic injection locking (SHIL) evolution of each individual STNO. The purpose of the second harmonic is to induce a binary injection locking²⁴, so that each STNO settles in one of two possible locking states²⁵, that can be distinguished based on their phase difference of π . Experimentally, regardless of the coupling mechanism, different techniques can be used to know the locking state of each individual oscillator. This is a mandatory requirement to evaluate the temporal evolution of the energy landscape of the Ising machine. One possible solution is to design a system where an individual access to the phase of each oscillator is achieved. From a fabrication point of view, this option is clearly more challenging in systems driven by a short-range coupling between oscillators. Houshang et al.²⁶ have recently shown a second solution for 2×2 arrays of short-range coupled spin Hall nano-oscillators, where the locking state of each oscillator is deduced from the variation of the output emission of the system when locked to the second harmonic.

In this work, a magneto-dipolar coupling between pairs of MgO-based magnetic tunnel junctions²⁷ (MTJs) working as STNOs in close proximity is complemented with individual electrical contacts to each device. MTJs are a technologically

mature spintronic building block and CMOS compatible²⁸, making them a viable candidate for emerging computing paradigms. The fabrication of adjacent STNOs with independent top contacts, not only provides access to the phase and frequency of each individual oscillator, but also makes possible to tune the current across each device and control their individual frequencies. This is not possible in the conventional geometry where dipolar coupled oscillators are implemented in a parallel configuration with a shared top and bottom electric contacts^{6,8}. With this design, two experiments were successfully achieved: (i) a clear demonstration of synchronization via dipolar coupling and (ii) the control of the SHIL to an external RF signal by changing the coupling between oscillators.

Results and discussion

Fabrication and characterization setup for vortex oscillators.

This work is based on circular nanopillars, patterned from an MgO-based MTJ stack (more details presented in the “Methods” section). Each nanopillar acts as a spin torque vortex oscillator (STVO), due to the patterning that induces a vortex magnetic state in the free layer.

To take advantage of the magneto-dipolar interaction, the nanopillars were defined in pairs with an edge-to-edge distance (d_{ee}) down to 100 nm. Figure 1a shows a scanning electron microscopy (SEM) image of an STVO pair with a nominal $d_{ee} = 100$ nm, after an electron-beam lithography and definition by ion beam milling. Instead of a standard top contact common to both STVOs^{6,8}, an extra electron-beam lithography was performed to define two individual top contacts (ITCs), as depicted in Fig. 1b.

Figure 1c shows an illustration of the experimental setup used to characterize the magneto-dynamic properties of the ITC devices. Independently through a bias tee, each source applies a DC current to each individual STVO. Then, the RF signal from the steady-state oscillation of each STVO is transmitted by the bias tee capacitor, allowing an analysis in the frequency and time domains. In the frequency domain, the spectrum analyser allows to collect the combined signals of both STVOs, whereas in the time domain, two independent oscilloscope channels allow to visualize both individual signals simultaneously. The setup also shows the existence of an integrated field line²⁹, patterned on top of the nanopillars during fabrication. In this work, the field line was used, not only to apply a local in-plane static field, but also for SHIL. Although not shown, a perpendicular magnetic field is also applied via an external electromagnet, as generally required to obtain vortex gyrotropic oscillations³⁰.

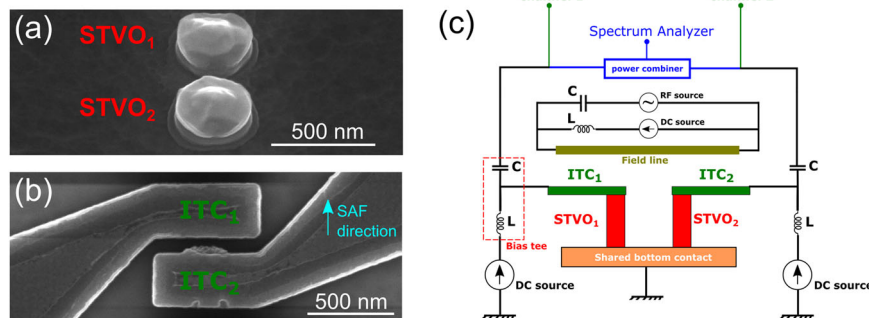


Fig. 1 Device layout. **a** Scanning electron microscopy (SEM) image obtained after dry etching definition for a pair of magnetic tunnel junctions (MTJs). The nanopillars have a nominal diameter of 300 nm and a nominal edge-to-edge (d_{ee}) distance of 100 nm. The image is obtained at a viewing angle of 40° with respect to the perpendicular direction. **b** Top view SEM image obtained after dry etching definition of a pair of individual top contacts (ITCs) establishing electric contact to a pair of MTJs with $d_{ee} = 100$ nm. The blue arrow indicates the pinning direction of the reference synthetic antiferromagnetic (SAF) structure. **c** Illustration of the experimental setup used for the characterization of MTJ nanopillars with independent top contacts.

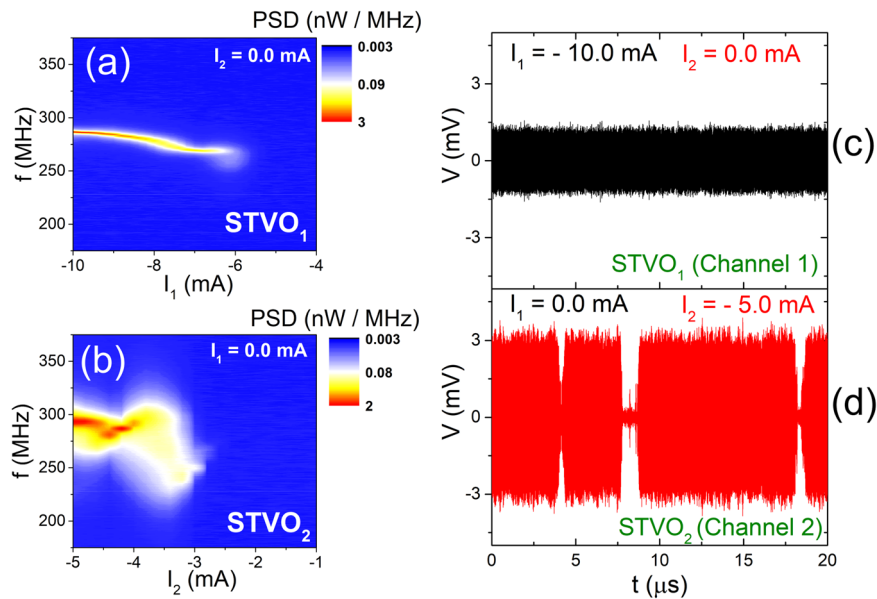


Fig. 2 Dynamics of individual oscillators. **a, b** Power spectral density (PSD) individually measured from two spin torque vortex oscillators (STVO₁ and STVO₂) with an edge-to-edge distance of 100 nm. **a** Spectrum obtained for STVO₁ as a function of the direct current I_1 (the direct current I_2 applied to STVO₂ is kept at zero). **b** Spectrum obtained for STVO₂ as a function of I_2 (I_1 is kept at zero). **c** Time trace obtained for STVO₁ at $I_1 = -10.0$ mA. **d** Time trace obtained for STVO₂ at $I_2 = -5.0$ mA. Each time trace is presented after application of a band pass filter between 150 MHz and 400 MHz to include only the gyrotropic oscillation. A perpendicular magnetic field of 2.8 kOe was applied during the measurements.

Synchronization via magneto-dipolar coupling. Figure 2 shows the individual dynamics of each oscillator in a pair of STVOs (STVO₁ and STVO₂) with $d_{ee} = 100$ nm and a diameter of 350 nm, observed both in frequency and time domains. In this first analysis, the dynamics of each STVO are individually measured, meaning that the DC bias current is only applied to one of the devices. In this work, a positive DC bias current corresponds to electrons travelling from the reference to the free layer. The spectra measured in the spectrum analyser are depicted in Fig. 2a, b for the DC current sweep of STVO₁ and STVO₂, respectively.

Although nominally similar, the two STVOs have different dynamic properties. STVO₁ shows a larger threshold current for gyrotropic oscillations, which may indicate a more degraded insulating barrier, i.e. a larger current needs to be applied to compensate the current spread through the conductive paths of the barrier³¹, or simply a slightly different diameter as a result of lithographic and ion milling induced dispersion. Moreover, the devices present small power emissions, with an output power density at the nW/MHz range. These results are justified by the small RA product of the MTJ stack ($3.67 \Omega \cdot \mu\text{m}^2$), which is too small to provide large output RF power. In fact, a too thin MgO barrier is more susceptible to defects as pinholes³² and amorphous regions³³, whose main consequences are the decrease of the spin-polarization of the DC bias current and a larger sample-to-sample variability.

STVO₂ shows a smaller threshold but a poorer spectral purity. The cause for this behaviour can be better understood by looking at the time trace obtained in the oscilloscope, shown in Fig. 2d. The vortex oscillation is not continuously sustained over a long time, in contrast with the time trace obtained for STVO₁ [Fig. 2c]. This behaviour has already been reported in the literature and tends to occur near the DC current threshold for vortex oscillations³⁴. Each STVO operates at distinct DC current windows because their different resistances dictate different maxima of the DC current that can be applied to avoid reaching the breakdown voltage.

After the characterization of each individual device, the synchronization between STVOs is evaluated by sweeping the

DC current of STVO₁ (I_1), while maintaining constant the DC current passing through STVO₂ (I_2). Thus, the coupling strength between the two STVOs is controlled by I_1 . The dynamics were measured in the frequency domain using the power combiner, as illustrated in Fig. 1c. The results are presented in Fig. 3a, where $I_2 = -5.0$ mA and I_1 is swept down to -10.0 mA. Upon reaching $I_1 \leq -6.0$ mA (which is the threshold current required to promote auto-oscillations of STVO₁), the output of the two oscillators is distinguishable in the frequency spectrum with a peak close to 300 MHz (from STVO₂) and a peak close to 275 MHz (from STVO₁). Increasing the current magnitude across STVO₁ results in a decrease of the frequency detuning between the two oscillators, until a clear frequency merging occurs for $I_1 \leq -8.2$ mA, where only a single peak is visible. Figures 3c, d show the linewidth and the output power, respectively, of the system for different conditions, in order to compare the performance of each individual oscillator (STVO₁ in black and STVO₂ in red) with the performance of both combined (in blue). The fundamental parameters that characterize the dynamics (i.e. frequency, linewidth and output power) are obtained from a Lorentzian fit performed to the single peak of each spectrum³⁵. This calculation was performed for the $I_1 \leq -8.2$ mA range, where the STVOs are oscillating at the same frequency and the synchronization is expected. In this analysis, since $I_2 = -5.0$ mA, the parameters of the STVO₂ single oscillation are constant over the full I_1 range. When both STVOs are oscillating, a clear improvement of the output power is verified [blue curve in Fig. 3d]. As an example, Fig. 3b shows the spectra obtained for $I_1 = -10.0$ mA and $I_2 = -5.0$ mA, for single (black and red) and combined (blue) dynamics. The output power increases to $P_{\text{SYNCH}} = 41.3$ nW, which is significantly larger than the sum of the powers of each STVO oscillating alone ($P_1 = 3.3$ nW and $P_2 = 22.2$ nW). Regarding the spectral coherence, the linewidth of the combined oscillation [blue curve in Fig. 3c] tends to merge to the values presented by STVO₁ [black curve in Fig. 3c], which means that only the noisiest oscillator STVO₂ shows a significant improvement of its spectral coherence, from 8.86 MHz [red dash line in Fig. 3c] to 966 kHz [blue data in

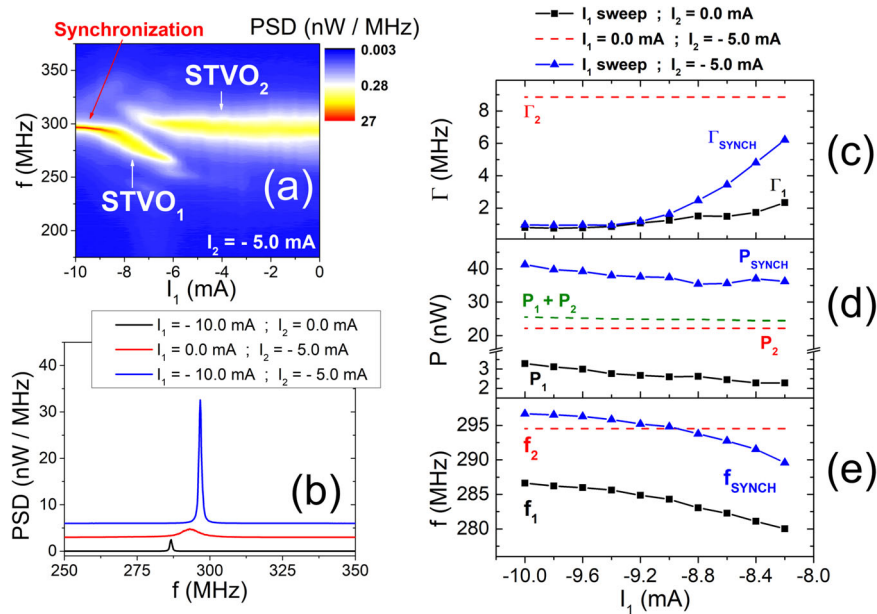


Fig. 3 Synchronization of two dipolar-coupled oscillators. **a** Power spectral density (PSD) measured for two spin torque vortex oscillators (STVO₁ and STVO₂) with an edge-to-edge distance of 100 nm, as a function of the direct current I_1 passing through STVO₁. The direct current I_2 applied to STVO₂ is -5.0 mA. **b** Example of the PSD obtained for $I_1 = -10.0$ mA and $I_2 = -5.0$ mA for single (black and red) and combined (blue) oscillations. **c** Linewidth, **d** output power and **e** frequency calculated as a function of I_1 for $I_2 = 0.0$ mA (black) and $I_2 = -5.0$ mA (blue). For an easy comparison, the parameters obtained for an isolated oscillation of STVO₂ at $I_2 = -5.0$ mA (red) are also shown without any connection with the I_1 axis. A perpendicular magnetic field of 2.8 kOe was applied during the measurements.

Fig. 3c, at $I_1 = -10.0$ mA]. The increase of the I_1 magnitude is also followed by an increase of the synchronized state frequency [f_{SYNCH} in Fig. 3e]. For $I_1 \leq -9.0$ mA, f_{SYNCH} goes above both f_1 and f_2 single-running frequencies of STVO₁ and STVO₂, respectively, which is a behaviour already verified in the literature for synchronized STVOs⁸. These results already demonstrate the fingerprint of a synchronization of the two STVOs^{7,9}, but they still lack the demonstration that the two oscillators are locked with a constant phase difference between them.

Thanks to the ITC geometry, direct access to the phase of each individual STVO is also possible, enabling a better understanding of the individual behaviour of each STVO in the synchronized state. The phase evolution can be measured using two independent oscilloscope channels connected to each oscillator, as depicted in Fig. 1c. After measuring the time trace $v(t)$ of an individual STVO, the instantaneous phase can be extracted from its analytic signal³⁶, given by³⁷

$$v_a(t) = v(t) + j\mathcal{H}[v(t)] = A(t)e^{j\Psi(t)} \quad (1)$$

where j is the imaginary unit, $\mathcal{H}[v(t)]$ the Hilbert transform of the time trace, $A(t)$ is the instantaneous amplitude and $\Psi(t)$ is the instantaneous phase of $v(t)$. This signal processing method has also been applied for the noise characterization of spin torque oscillators^{24,34,37,38}. For each value of I_1 , the dynamics of each oscillator are measured independently in the time domain, so that it is possible to extract the instantaneous phases $\Psi_1(t)$ for STVO₁ and $\Psi_2(t)$ for STVO₂. If the two oscillators are truly locked in a synchronized state, the phase difference between the two must be constant over time, i.e. $\Delta\Psi(t) = \Psi_1(t) - \Psi_2(t) = \text{constant}$.

Figure 4a shows $\Delta\Psi$ calculated from 40 μs time traces and for different values of I_1 . In addition to the frequency domain analysis of Fig. 3, these results demonstrate a successful synchronization in a mutually locked state. The system evolves from an unsynchronized state, e.g. $I_1 = -7.4$ mA where $\Delta\Psi$ diverges in time, to a stable synchronization at $I_1 = -8.6$ mA, that is maintained down to $I_1 = -10.0$ mA. The time domain analysis

gives some details that cannot be clarified by the frequency domain measurements depicted in Fig. 3. Considering the measurement period of 40 μs , the phase evolution shows that a stable synchronization is only achieved for $I_1 \leq -8.6$ mA. The output power calculated in Fig. 3d suggests a synchronization state starting at $I_1 = -8.2$ mA. In fact, at the $-8.6 \text{ mA} < I_1 < -8.0$ mA range (i.e. at the edge of the frequency synchronization bandwidth), Fig. 4a shows that the mutual coupling between the two oscillators is not strong enough to ensure phase locking of the two oscillators within the time window of 40 μs , despite being strong enough to pull both oscillators to the same frequency value. In this region, $\Delta\Psi$ shows stable periods separated by desynchronization-resynchronization events, as shown in Fig. 4b, characterized by phase slips of $2\pi n$ (with n being an integer) which, considering the STVOs frequency synchronization, indicate a single synchronization state per period²⁴. In Fig. 3, the consequences of such an unstable state, characterized by transient phase-slip events, are particularly visible in the spectral linewidth of the synchronized state [blue data in Fig. 3c] that, in this region, is still far away from the values obtained for $I_1 \leq -8.6$ mA. Regarding the output power [Fig. 3d], that influence is not so significant, since P_{synch} is much larger than the sum of P_1 and P_2 over the full I_1 range. The existence of phase slips between the two oscillators is also visible in the unsynchronized state for $I_1 \geq -8.0$ mA, with much shorter stable periods and more pronounced divergence in time.

Another important aspect to consider is that $\Delta\Psi$ of the synchronized state is a non-trivial value, i.e. neither zero, nor π . To avoid any artificial contribution to $\Delta\Psi$, each STVO is connected to the measurement instrumentation by RF cables with the exact same length. In Fig. 4c, the synchronization is characterized by $\Delta\Psi = -0.9 \pm 0.2$ (rad) [$\Delta\Psi = -49 \pm 9$ ($^\circ$)]. In fact, if two identical STVOs are considered, the theory predicts a synchronized state, via magneto-dipolar interaction, with $\Delta\Psi = 0$ or $\Delta\Psi = \pi$, depending on the magnetic parameters of the vortices^{39,40}. On the other hand, for non-identical oscillators,

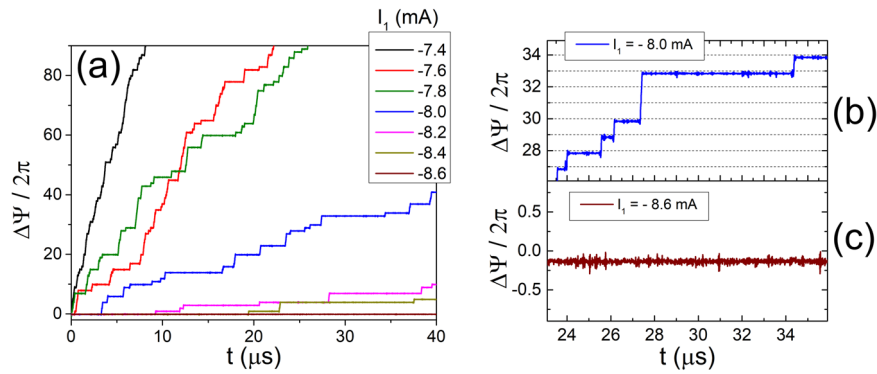


Fig. 4 Phase evolution of two dipolar-coupled oscillators. **a** The instantaneous phase difference ($\Delta\Psi$) is presented as a function of time, for different values of the direct current I_1 passing through oscillator 1 (STVO₁). The direct current passing through oscillator 2 (STVO₂) is -5.0 mA. $\Delta\Psi$ is zoomed in for **(b)** $I_1 = -8.0$ mA and **(c)** $I_1 = -8.6$ mA. A perpendicular magnetic field of 2.8 kOe was applied during the measurements.

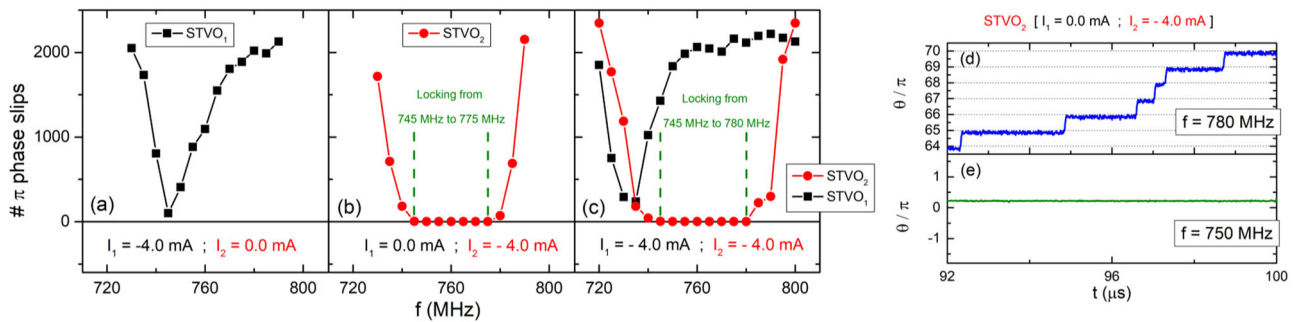


Fig. 5 Second harmonic injection locking of two dipolar-coupled oscillators. The quality of second harmonic injection locking (SHIL) is presented by calculating the number of π phase slips as a function of the frequency of the external signal. The locking is quantified for **(a)** oscillator 1 (STVO₁), **(b)** oscillator 2 (STVO₂) and **(c)** both when frequency tuned. Two examples of the phase deviation of STVO₂ are presented for two distinct frequencies of the external signal applied through the field line: **(d)** 780 MHz and **(e)** 750 MHz. These measurements were obtained with a direct current of -66 mA and a radio-frequency power of 10 mW, both applied through the field line.

the theory shows that a non-trivial $\Delta\Psi$ is possible^{41,42}. In this experiment, the two STVOs under study are clearly non-identical, as shown by their individual dynamics in Fig. 2. The source of this sample-to-sample variability is most probably a combination of different factors, arising from the limitations of the fabrication process (e.g. lithographic accuracy, uniformity of the MgO barrier deposition), as oscillators with different spin torque parameters⁴² or with a diameter mismatch⁴¹.

SHIL to an external source mediated and tuned by magneto-dipolar coupling to a second oscillator. The second harmonic injection can be easily implemented with the setup of Fig. 1c, using the integrated field line to apply an RF signal with twice the frequency of the coupled STVOs. The aim is to study the second harmonic injection locking (SHIL) of two dipolar coupled STVOs. A pair of functional STVOs (diameter of 350 nm) with $d_{ee} = 400$ nm were investigated. Although full synchronization is not achieved [see Fig. S3b in the supplementary], a dipolar coupling between STVOs still exists³⁹.

Instead of merging the dynamics by sweeping the DC current of one of the oscillators, as performed in Fig. 3, the DC current passing through each nanopillar was kept constant and the integrated field line [see Fig. 1c] was used to apply a common in-plane magnetic field along the MTJ easy axis, sweeping the DC current through the field line. This method was used to ensure that the two STVOs, showing very distinct dynamics and a weak magneto-dipolar coupling, can effectively be merged to operate at the same frequency [see Fig. S3a in the supplementary].

SHIL was studied in the time domain for these two weakly coupled STVOs, using the two individual channels of the oscilloscope [see Fig. 1c]. The second harmonic of each oscillator ($2.f_{\text{STVO}}$) should be synchronized with an external RF signal (f_{SH}) which, in this case, is also injected through the field line. With perfect SHIL, the phase deviation of each STVO $\theta(t) = \psi(t-t_0) - 2\pi.f_{\text{STVO}}.t$ must be constant over time, being $\psi(t_0)$ the instantaneous phase of each oscillator at a reference point in time and f_{STVO} its frequency. One important difference of SHIL with respect to the dipolar coupling locking described in the previous section is that there are two possible locking configurations between the oscillators and the external RF signal. This happens because during one period of an STVO oscillation, there are two different points in time where the phase of the external RF signal matches the phase of the STVO. These two points in time are separated by the period of oscillation of the external RF signal. Since this period is half of the period of the oscillators, these two possible phase locking points are separated by a value of π in terms of the oscillator phase. For this reason, in a SHIL mechanism with a non-perfect phase locking, it is possible to observe phase slips corresponding to phase differences that are integer values of π ²².

A simple method to quantify SHIL is to count the number of phase slips in 100 μs time traces, shown in Fig. 5a–c, as a function of the frequency of the RF signal (with an input power of 10 mW) injected through the field line. At a constant DC current of -66 mA passing through the field line, this analysis is performed for individual [STVO₁ in Fig. 5a for $I_1 = -4.0$ mA and $I_2 = 0.0$ mA; STVO₂ in Fig. 5b for $I_1 = 0.0$ mA and $I_2 = -4.0$ mA] and

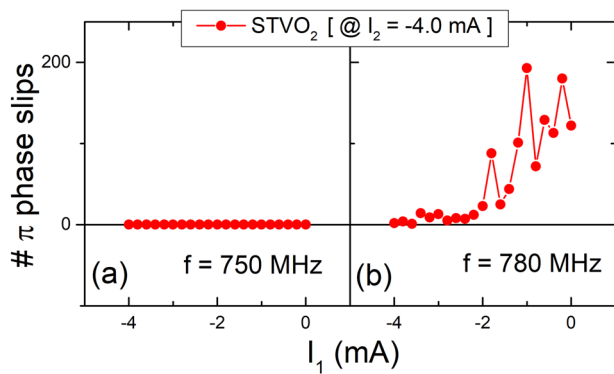


Fig. 6 Variation of the locking with the coupling between oscillators. The second harmonic injection locking (SHIL) of oscillator 2 (STVO₂) is calculated by its π phase slips, presented as a function of the direct current I_1 applied to oscillator 1 (STVO₁) for two distinct frequencies of the external signal: (a) 750 MHz and (b) 780 MHz. The direct current I_2 applied to STVO₂ is -4.0 mA.

frequency tuned [Fig. 5c for $I_1 = I_2 = -4.0$ mA] oscillations and shows the locking between each STVO and the RF signal.

Regarding the individual locking, the STVOs show different behaviours. In Fig. 5b, STVO₂ shows an efficient SHIL from 745 MHz to 775 MHz (i.e. zero phase slips). Figure 5d, e show two examples of the normalized θ/π of STVO₂: when perfectly locked [Fig. 5e at 750 MHz] and outside the locking range [Fig. 5d at 780 MHz, characterized by phase slips]. On the other hand, STVO₁ is never perfectly locked, showing phase slips for the full frequency range [Fig. 5a]. These results are justified by the different spectral purities presented by each STVO before locking [see Fig. S3(c) of the supplementary]. These results are in accordance with the work of Hamadeh et al., where it is demonstrated that the locking quality (i.e. linewidth of the locked state and locking range) of an STVO to an external RF field depends on the spectral coherence of its individual oscillation⁴³. So, the larger linewidth presented by STVO₁ naturally leads to a poorer locking range. The results are qualitatively the same in Fig. 5c, where the locking of STVO₂ is not followed by STVO₁. Nevertheless, the dynamics of STVO₁ change the SHIL range of STVO₂—now from 745 MHz to 780 MHz—as a result of the weak magneto-dipolar coupling between the pair.

After understanding the behaviour of each STVO to the second harmonic injection, it is important to investigate how the dipolar coupling affects the locking. In an oscillator-based Ising machine^{44–46}, the annealing process performed to evolve the system to its energy minimum includes a schedule, not only of the external second harmonic, but also of the coupling strength between the oscillators²⁵. The ability to manipulate the coupling strength between the two oscillators coupled by a SHIL mechanism is an essential requirement for the implementation of an Ising machine. In our system, the coupling strength between the STVOs can be controlled by an additional degree of freedom with respect to the fixed geometry of the ITC design: the DC bias current of each STVO. To illustrate this fact, the phase slips of the STVO₂ were measured as a function of the DC bias current applied to the poorly locked STVO₁.

Figure 6 shows the π phase slips, translating the quality of the locking between STVO₂ and the external RF signal, as a function of the DC current applied to STVO₁. This analysis is performed for two distinct frequencies of the external signal: (i) 750 MHz, inside the locking range of STVO₂ and (ii) 780 MHz, at the edge of that same locking range [see Fig. 5b]. At 750 MHz [Fig. 6a], STVO₂ is strongly locked with its second harmonic, meaning that the dipolar coupling tuned by I_1 has no influence in the locking state. On the other hand, at 780 MHz [Fig. 6b], the coupling between STVO₂ and

the external source is already very weak [i.e. non-zero phase slips in Fig. 5b at 780 MHz], which means that the magneto-dipolar coupling between STVO₁ and STVO₂ is now strong enough to determine whether STVO₂ is capable to phase lock to the second harmonic of the external RF signal or not. The increase of the I_1 magnitude is followed by a decrease of the phase slips, making the SHIL of STVO₂ more robust, which is in accordance with the increase of its locking range⁴⁷ up to 780 MHz in Fig. 5c for $I_1 = -4.0$ mA. This locking improvement is justified by the variation of the STVO₂ frequency with the I_1 sweep, that changes the detuning between STVO₂ and the external RF signal [see Fig. S4 of the supplementary and also the details described in “supplementary note 1” of the supplementary]. In summary, the SHIL mechanism implemented in an ITC geometry with a pair of magneto-dipolar coupled STVOs has the functional properties required to implement the basic building block of an Ising machine.

Conclusions

A nanofabrication design was successfully implemented for the synchronization of an STVO pair with an edge-to-edge distance of 100 nm, via magneto-dipolar coupling. Each nanopillar is electrically accessible through an independent top contact, allowing a direct access to its individual phase. Moreover, the coupling strength between oscillators can be tuned by the DC current passing through each individual oscillator. It was also verified experimentally that the SHIL between an STVO and an external signal can be manipulated by tuning the coupling strength to the other STVO of the same pair, with an edge-to-edge distance of 400 nm. This work opens new perspectives for the integration of coupled STVOs in unconventional computing hardware, as oscillator-based Ising machines, providing that their time domain dynamics can be individually analysed and that their coupling can be efficiently controlled.

Methods

Details of the oscillator stack. The devices under investigation are circular nanopillars with diameters of 300 nm and 350 nm, patterned from a 6.0 IrMn / 2.6 CoFe₃₀ / 0.85 Ru / 1.8 CoFe₄₀B₂₀ / MgO / 2.0 CoFe₄₀B₂₀ / 0.2 Ta / 7.0 NiFe₁₉ MTJ stack (thickness in nanometers). The full stack corresponds to “Stack A” presented in Table S1 of the supplementary. From current in-plane tunnelling (CIPT) measurements⁴⁸, the thickness of the MgO barrier dictates a resistance-area (RA) product of 3.67 $\Omega \cdot \mu\text{m}^2$. The composite free layer is constituted by the 2.0 CoFe₄₀B₂₀ / 0.2 Ta / 7.0 NiFe₁₉ structure, where the two magnetic layers are coupled into a remanent vortex state⁴⁹ upon the patterning of the stack into nanopillars. Before any electrical characterization, the devices were subjected to an annealing treatment described elsewhere⁵⁰.

Fabrication yield. After fabrication, all the devices were individually tested in what concerns their static magneto-transport properties (i.e. resistance versus in-plane magnetic field transfer curve) to calculate the yield of the process as a function of d_{ee} (see Fig. S1 of the supplementary information). The results show a decrease of the yield as d_{ee} decreases. This tendency is strictly related with the limits of the fabrication process (see Fig. S3 of the supplementary information). Nevertheless, the process delivers functional STVOs even for the smallest d_{ee} designed in this work (yield of 35% for $d_{ee} = 100$ nm).

Data availability

The data supporting this scientific work are available from the corresponding author upon reasonable request.

Received: 13 October 2022; Accepted: 6 April 2023;

Published online: 15 April 2023

References

1. Mancoff, F. B., Rizzo, N. D., Engel, B. N. & Tehrani, S. Phase-locking in double-point-contact spin-transfer devices. *Nature* **437**, 393–395 (2005).

2. Kaka, S. et al. Mutual phase-locking of microwave spin torque nano-oscillators. *Nature* **437**, 389–392 (2005).
3. Ruotolo, A. et al. Phase-locking of magnetic vortices mediated by antivortices. *Nat. Nanotechnol.* **4**, 528–532 (2009).
4. Sani, S. et al. Mutually synchronized bottom-up multi-nanocontact spin-torque oscillators. *Nat. Commun.* **4**, 2731 (2013).
5. Houshang, A. et al. Spin-wave-beam driven synchronization of nanocontact spin-torque oscillators. *Nat. Nanotechnol.* **11**, 280–286 (2016).
6. Locatelli, N. et al. Efficient synchronization of dipolarly coupled vortex-based spin transfer nano-oscillators. *Sci. Rep.* **5**, 17039 (2015).
7. Lebrun, R. et al. Mutual synchronization of spin torque nano-oscillators through a long-range and tunable electrical coupling scheme. *Nat. Commun.* **8**, 15825 (2017).
8. Li, Y. et al. Selective control of vortex polarities by microwave field in two robustly synchronized spin-torque nano-oscillators. *Appl. Phys. Lett.* **112**, 022405 (2018).
9. Tsunegi, S. et al. Scaling up electrically synchronized spin torque oscillator networks. *Sci. Rep.* **8**, 13475 (2018).
10. Jenkins, A. S. et al. Phase variation in the locked state of mutually synchronized spin torque nano-oscillators. *Appl. Phys. Lett.* **118**, 172406 (2021).
11. Chang, H.-C., Cao, X., Mishra, U. K. & York, R. A. Phase noise in coupled oscillators: theory and experiment. *IEEE Trans. Microw. Theory Tech.* **45**, 604–615 (1997).
12. Grollier, J., Cros, V. & Fert, A. Synchronization of spin-transfer oscillators driven by stimulated microwave currents. *Phys. Rev. B* **73**, 060409 (2006).
13. Zahedinejad, M. et al. Two-dimensional mutually synchronized spin Hall nano-oscillator arrays for neuromorphic computing. *Nat. Nanotechnol.* **15**, 47–52 (2020).
14. Sharma, R. et al. Electrically connected spin-torque oscillators array for 2.4 GHz WiFi band transmission and energy harvesting. *Nat. Commun.* **12**, 2924 (2021).
15. Grollier, J. et al. Neuromorphic spintronics. *Nat. Electron.* **3**, 360–370 (2020).
16. Torrejon, J. et al. Neuromorphic computing with nanoscale spintronic oscillators. *Nature* **547**, 428–431 (2017).
17. Romera, M. et al. Vowel recognition with four coupled spin-torque nano-oscillators. *Nature* **563**, 230–234 (2018).
18. Marković, D. et al. Reservoir computing with the frequency, phase, and amplitude of spin-torque nano-oscillators. *Appl. Phys. Lett.* **114**, 012409 (2019).
19. Tsunegi, S. et al. Physical reservoir computing based on spin torque oscillator with forced synchronization. *Appl. Phys. Lett.* **114**, 164101 (2019).
20. Leroux, N. et al. Hardware realization of the multiply and accumulate operation on radio-frequency signals with magnetic tunnel junctions. *Neuromorphic Comput. Eng.* **1**, 011001 (2021).
21. Albertsson, D. I. et al. Ultrafast Ising Machines using spin torque nano-oscillators. *Appl. Phys. Lett.* **118**, 112404 (2021).
22. Lucas, A. Ising formulations of many NP problems. *Front. Phys.* **2**, 1–14 (2014).
23. McMahan, P. L. et al. A fully programmable 100-spin coherent Ising machine with all-to-all connections. *Science* **354**, 614–617 (2016).
24. Lebrun, R. et al. Understanding of phase noise squeezing under fractional synchronization of a nonlinear spin transfer vortex oscillator. *Phys. Rev. Lett.* **115**, 017201 (2015).
25. Wang, T., Wu, L., Nobel, P. & Roychowdhury, J. Solving combinatorial optimisation problems using oscillator based Ising machines. *Nat. Comput.* **20**, 287–306 (2021).
26. Houshang, A. et al. Phase-binarized spin hall nano-oscillator arrays: towards spin hall ising machines. *Phys. Rev. Appl.* **17**, 014003 (2022).
27. Yuasa, S. & Djayaprawira, D. D. Giant tunnel magnetoresistance in magnetic tunnel junctions with a crystalline MgO(001) barrier. *J. Phys. D: Appl. Phys.* **40**, R337–R354 (2007).
28. Jung, S. et al. A crossbar array of magnetoresistive memory devices for in-memory computing. *Nature* **601**, 211–216 (2022).
29. Jenkins, A. S. et al. Wideband high-resolution frequency-to-resistance converter based on nonhomogeneous magnetic-state transitions. *Phys. Rev. Appl.* **13**, 014046 (2020).
30. Dussaux, A. et al. Large microwave generation from current-driven magnetic vortex oscillators in magnetic tunnel junctions. *Nat. Commun.* **1**, 8 (2010).
31. Costa, J. D. et al. High power and low critical current density spin transfer torque nano-oscillators using MgO barriers with intermediate thickness. *Sci. Rep.* **7**, 7237 (2017).
32. Ventura, J. et al. Pinholes and temperature-dependent transport properties of MgO magnetic tunnel junctions. *Phys. Rev. B* **78**, 024403 (2008).
33. Yuasa, S., Suzuki, Y., Katayama, T. & Ando, K. Characterization of growth and crystallization processes in CoFeBMgOCoFeB magnetic tunnel junction structure by reflective high-energy electron diffraction. *Appl. Phys. Lett.* **87**, 1–3 (2005).
34. Grimaldi, E. et al. Response to noise of a vortex based spin transfer nano-oscillator. *Phys. Rev. B* **89**, 104404 (2014).
35. Dussaux, A. et al. Large amplitude spin torque vortex oscillations at zero external field using a perpendicular spin polarizer. *Appl. Phys. Lett.* **105**, 022404 (2014).
36. Picinbono, B. On instantaneous amplitude and phase of signals. *IEEE Trans. Signal. Process.* **45**, 552–560 (1997).
37. Bianchini, L. et al. Direct experimental measurement of phase-amplitude coupling in spin torque oscillators. *Appl. Phys. Lett.* **97**, 032502 (2010).
38. Quinsat, M. et al. Amplitude and phase noise of magnetic tunnel junction oscillators. *Appl. Phys. Lett.* **97**, 182507 (2010).
39. Belanovsky, A. D. et al. Phase locking dynamics of dipolarly coupled vortex-based spin transfer oscillators. *Phys. Rev. B* **85**, 100409(R) (2012).
40. Abreu Araujo, F. et al. Optimizing magnetodipolar interactions for synchronizing vortex based spin-torque nano-oscillators. *Phys. Rev. B* **92**, 1–8 (2015).
41. Belanovsky, A. D. et al. Numerical and analytical investigation of the synchronization of dipolarly coupled vortex spin-torque nano-oscillators. *Appl. Phys. Lett.* **103**, 122405 (2013).
42. Chen, H. H. et al. Phase locking of spin-torque nano-oscillator pairs with magnetic dipolar coupling. *Phys. Rev. B* **93**, 224410 (2016).
43. Hamadeh, A. et al. Perfect and robust phase-locking of a spin transfer vortex nano-oscillator to an external microwave source. *Appl. Phys. Lett.* **104**, 022408 (2014).
44. McGoldrick, B. C., Sun, J. Z. & Liu, L. Ising machine based on electrically coupled spin hall nano-oscillators. *Phys. Rev. Appl.* **17**, 014006 (2022).
45. Zhang, Y. et al. Oscillator-network-based ising machine. *Micromachines* **13**, 1016 (2022).
46. Mohseni, N., McMahon, P. L. & Byrnes, T. Ising machines as hardware solvers of combinatorial optimization problems. *Nat. Rev. Phys.* **4**, 363–379 (2022).
47. Romera, M. et al. Enhancing the injection locking range of spin torque oscillators through mutual coupling. *Appl. Phys. Lett.* **109**, 252404 (2016).
48. Worledge, D. C. & Troulloud, P. L. Magnetoresistance measurement of unpatterned magnetic tunnel junction wafers by current-in-plane tunneling. *Appl. Phys. Lett.* **83**, 84 (2003).
49. Guslienko, K. Y. Magnetic vortex state stability reversal and dynamics in restricted geometries. *J. Nanosci. Nanotechnol.* **8**, 2745–2760 (2008).
50. Martins, L. et al. Non-volatile artificial synapse based on a vortex nano-oscillator. *Sci. Rep.* **11**, 16094 (2021).

Acknowledgements

L.M. would like to thank FCT—Fundação Ciência e Tecnologia—for support concerning his PhD grant SFRH/BD/128833/2017. This work has received funding from the European Union’s Horizon 2020 research and innovation programme under grant agreement No 101017098 (project RadioSpin) and grant agreement No 899559 (project SpinAge).

Author contributions

The MTJ devices were fabricated by L.M., being J.B. responsible for the definition of the nanopillars by e-beam lithography. The manuscript was written by L.M. and reviewed by A.S.J., J.V. and R.F. The first author L.M. performed the experimental measurements. A.S.J. performed the micromagnetic simulations. J.V., P.P.F. and R.F. were responsible for the scientific coordination of the work.

Competing interests

The authors declare no competing interests.

Additional information

Supplementary information The online version contains supplementary material available at <https://doi.org/10.1038/s42005-023-01200-5>.

Correspondence and requests for materials should be addressed to Alex S. Jenkins.

Peer review information *Communications Physics* thanks Raghav Sharma, Zhongrui Wang and the other, anonymous, reviewer(s) for their contribution to the peer review of this work. Peer reviewer reports are available.

Reprints and permission information is available at <http://www.nature.com/reprints>

Publisher’s note Springer Nature remains neutral with regard to jurisdictional claims in published maps and institutional affiliations.



Open Access This article is licensed under a Creative Commons Attribution 4.0 International License, which permits use, sharing, adaptation, distribution and reproduction in any medium or format, as long as you give appropriate credit to the original author(s) and the source, provide a link to the Creative Commons license, and indicate if changes were made. The images or other third party material in this article are included in the article's Creative Commons license, unless indicated otherwise in a credit line to the material. If material is not included in the article's Creative Commons license and your intended use is not permitted by statutory regulation or exceeds the permitted use, you will need to obtain permission directly from the copyright holder. To view a copy of this license, visit <http://creativecommons.org/licenses/by/4.0/>.

© The Author(s) 2023